

A deterministic solver for a hybrid quantum-classical transport model in nanoMOSFETs

N. Ben Abdallah^a, M.J. Cáceres^b, J.A. Carrillo^{c,*}, F. Vecil^d

^aInstitut de Mathématiques, Université de Toulouse, Université Paul Sabatier, France

^bDepartamento de Matemática Aplicada, Universidad de Granada, Spain

^cICREA and Departament de Matemàtiques, Universitat Autònoma de Barcelona, E-08193 Bellaterra, Spain

^dJohann Radon Institute for Computational and Applied Mathematics (RICAM), Österreichische Akademie der Wissenschaften, Linz, Austria

ARTICLE INFO

Article history:

Received 7 February 2009

Received in revised form 28 April 2009

Accepted 4 June 2009

Available online 10 June 2009

PACS:

73.63.-b

73.23.-v

72.15.Lh

85.30.Tv

85.35.Be

Keywords:

Sub-band decomposition

PWENO interpolations

Semi-lagrangian methods

Quantum-classical dimensional coupling

Schrödinger–Poisson system

ABSTRACT

We model a nanoMOSFET by a mesoscopic, time-dependent, coupled quantum-classical system based on a sub-band decomposition and a simple scattering operator. We first compute the sub-band decomposition and electrostatic force field described by a Schrödinger–Poisson coupled system solved by a Newton–Raphson iteration using the eigenvalue/eigenfunction decomposition. The transport in the classical direction for each sub-band modeled by semiclassical Boltzmann-type equations is solved by conservative semi-lagrangian characteristic-based methods. Numerical results are shown for both the thermodynamical equilibrium and time-dependent simulations in typical nowadays nanoMOSFETs.

© 2009 Elsevier Inc. All rights reserved.

1. Introduction

In the typical structure of a nanoscaled double gate metal oxide semiconductor field effect transistor (DG-MOSFET) the electrons are confined along one dimension, called *confinement direction* or *transversal direction*, by two layers of silicon oxide. As the built-in potential at the Si–SiO₂ heterojunctions produces a well whose length is comparable to the Debye length, quantum effects play a relevant rôle, and thus, the energy levels, called *sub-bands* in the physical literature, become discrete and the probability density function (pdf) is decomposed into independent populations, one for each sub-band taken into account. Along the *longitudinal direction*, called *transport direction*, the electrons inside each sub-band flow from the source to the drain thanks to the applied bias and are assumed to be transported classically under Newton laws and interact quantum-mechanically with the crystal lattice. By assuming that the pdf is invariant along the remaining direction, we obtain a 2D model.

* Corresponding author. Fax: +34 58 243286.

E-mail address: carrillo@mat.uab.es (J.A. Carrillo).

One approach for the modelling of such a device, sketched in Fig. 1, is the use of a different description of the electrons following the dimension [6–8,35]: they behave as waves along the confinement direction (z -direction) and as particles along the transport direction (x -direction). This kind of coupling goes by the name of *dimensional coupling*, to differentiate it by the *geometrical coupling*, where different zones of the device are described by different models put together by interface conditions [4,5,21].

The dimensional coupling is justified because the behavior of the electrons along the confinement direction is quasi-static with respect to the transport direction, i.e., the time they need to achieve the equilibrium as waves is much smaller than the time they need to be transported inside the crystal. Therefore, their state as quantum objects is described by the stationary-state Schrödinger equation

$$H[V]\chi_p[V] = \epsilon_p[V]\chi_p[V], \quad (1)$$

where $H[V]$ is the one-dimensional Hamiltonian along the confinement

$$H[V] = H_z[V] = -\frac{\hbar^2}{2} \frac{d}{dz} \left(\frac{1}{m_*} \frac{d}{dz} \right) - q(V + V_c),$$

and $V(x, z)$ is the self-consistent potential with $z \in [0, L_z]$. Here, $V_c(z)$ represents the built-in potential drop, or *confining potential*, at the Si/SiO₂-heterojunctions producing the quantum well trapping the electrons; in our computations $V_c(z) = 3.15$ eV in the Si oxide layers and $V_c(z) = 0$ eV in the rest.

The eigenvalues $\{\epsilon_p[V]\}_p$ form a real, strictly increasing and tending to infinity set because this is a 1D Sturm–Liouville problem in a compact set $[0, L_z]$. This decomposition is what we have already introduced as *sub-band decomposition*. Should z not be confined, the spectrum might have continuous components and the sub-bands might not be separated.

The solution of (1) for each slice of the device gives the eigenvalues as a function of the unconfined direction $x \in [0, L_x] : \{\epsilon_p = \epsilon_p[V](x)\}_p$, while the eigenvectors $\{\chi_p = \chi_p[V](x, z)\}_p$ form an orthonormal basis for $L^2(0, L_z)$. We next take into account the electrostatic interaction through the Poisson equation

$$-\text{div}(\epsilon_R \nabla V) = -\frac{q}{\epsilon_0} (N[V] - N_D), \quad (2)$$

where $N[V]$ is the total electron density and N_D is the doping profile which takes into account the injected impurities in the semiconductor lattice. We now describe the transport in the classical direction by a set of Boltzmann transport equations (BTEs):

$$\frac{\partial f_p}{\partial t} + \frac{1}{\hbar} \nabla \epsilon_p^{\text{kin}} \cdot \nabla_x f_p - \frac{1}{\hbar} \nabla \epsilon_p \cdot \nabla_k f_p = \mathcal{Q}_p[f], \quad (3)$$

where $f_p(t, x, k)$ measures the probability density of finding an electron of the p th-subband at time t in position x with wave vector k . Here, the first part of the operator takes into account the classical transport of the electrons in each sub-band due to Newton's laws and the right-hand side, called the scattering operator, describes the interaction of the electrons with the crystal lattice and their possible sub-band jump. The band structure of the semiconductor crystal, also called the electron kinetic energy, is given in the one-valley case and under the parabolic approximation by

$$\epsilon_p^{\text{kin}}(k) = \frac{\hbar^2 |k|^2}{2m_*}.$$

We remark that Eqs. (1) and (2) are coupled because we need the potential V to compute the spectral elements $\{\epsilon_p, \chi_p\}_p$, and conversely the spectral elements are needed to compute the density $N[V]$ and subsequently the potential V . The total volume density $N[V]$ is a mixed quantum-classical state, apart from the sub-bands, it also couples the dimensions,

$$N(t, x, z) = \sum_{p=1}^{\infty} \rho_p(t, x) |\chi_p[V](t, x, z)|^2. \quad (4)$$

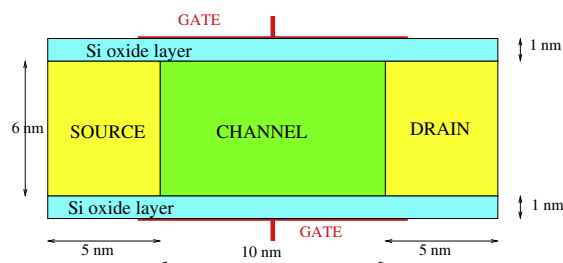


Fig. 1. The typical geometry of a DG-MOSFET: silicon oxide layers confine the carriers along the transversal direction.

Remark that the homogeneity of N is m^{-3} : the classical m^{-2} -contribution from the *surface densities*

$$\rho_p(t, \mathbf{x}) = \int_{\mathbb{R}^2} f_p(t, \mathbf{x}, k) dk,$$

and the quantum m^{-1} -contribution from the eigenfunctions $|\chi_p[V](t, \mathbf{x}, z)|^2$. Finally, we consider a simple relaxation time operator inside each sub-band given by

$$\mathcal{Q}_p[f](\mathbf{x}, k) = \frac{1}{\tau} (\rho_p(\mathbf{x})M(k) - f_p(\mathbf{x}, k)),$$

with

$$M(k) = \frac{\hbar^2}{2\pi m_* k_B T_L} \exp\left(-\frac{\hbar^2 |k|^2}{2m_* k_B T_L}\right),$$

and the relaxation time τ calculated by means of a given mobility μ : $\tau = \frac{\mu m_*}{q}$. Here, the effective mass m_* is set $0.5 m_e$, an average value between the longitudinal and the transversal Si effective masses. The rest of parameters which appear in the Boltzmann–Schrödinger–Poisson system Eqs. (1)–(4) are physical constants detailed in Table B.1.

These sub-band decomposition models are widely used in the electronic engineering community, see for instance [1,2,17,36], where the transport phase is solved by MonteCarlo-type methods. From the mathematical point of view, the connection of a full 2D Schrödinger–Poisson description of the electron transport to this sub-band decomposition in the confining direction was shown in [10] under a suitable rescaling limit involving the lengths L_x and L_z without taking into account the electron scatterings. As usual, this kinetic description is computationally expensive due to its high dimensionality. Therefore, in the literature one can find several approximated descriptions based on drift-diffusion, energy-transport or moment like models [6–8,18,35] obtained from diffusion-type scalings [9,26,29,30].

The main objective of this work is to develop an accurate fully deterministic method to solve the coupled Boltzmann–Schrödinger–Poisson system Eqs. (1)–(4). The numerical solver consists of a Schrödinger–Poisson (SP) block to compute the sub-band energies and the potential and a transport/collision phase to compute the electron densities of each sub-band. For the SP block we have used a Newton–Raphson algorithm which was first proposed by Nier for the one-dimensional Schrödinger–Poisson system [31] (see also [16,32,34]). This Newton–Raphson algorithm performs faster than Gummel iteration schemes in our out-of-equilibrium situation, see Section 4. The transport/collision phase is solved either by mass-preserving semi-lagrangian schemes [15,22] or by highly-accurate finite-difference schemes [12,13] using WENO interpolation for reconstructing flux or pointwise values. The semi-lagrangian scheme allows for larger time-stepping than the finite-difference method since there is no CFL condition while the finite-differences method is more accurate in time than the semi-lagrangian method. Other methods can be used for the transport/collision part as the multi-group methods proposed in [23,24].

The resulting scheme is a fully deterministic out-of-equilibrium time-dependent solver of the Boltzmann–Schrödinger–Poisson system Eqs. (1)–(4). The advantages of fully deterministic schemes compared to Monte-Carlo solvers available can be summarized analogously to the case of semiclassical Boltzmann–Poisson solvers [12–14,23–25] as:

- They allow for noise-free computation of the evolution on time of the distribution function at every point of the device and consequently all the macroscopic quantities, i.e., moments of the distribution function, and their stabilization trend towards the steady state.
- They actually represent benchmarks for hydrodynamic or drift-diffusion solvers that can fairly be tested against it.
- Almost-empty areas of the device are well-described. These areas are usually hard to compute for Monte Carlo solvers to obtain relevant information on density, mean velocity and energy.

The main drawback of this method with respect to MonteCarlo techniques is its computational cost which can be eased by parallelization techniques [28].

In this work, we have concentrated our efforts in setting up numerical techniques for dealing with a fast and accurate computation of the Schrödinger–Poisson and the transport phases. The collision operator has been kept as a simple relaxation, with constant in space relaxation time due to the constant in space mobility, and the electron band structure has been reduced to a single valley in the parabolic approximation for simplicity. We are currently incorporating realistic scattering operators and a more realistic band structure for Si devices to be reported in forthcoming works.

The paper is structured as follows: in Section 2 we present the initial and boundary conditions considered for this typical nanoMOSFET devices described by the system Eqs. (1)–(4). Section 3 is devoted to detail all parts of the numerical scheme. Finally, Section 4 validates the numerical scheme by computing equilibrium situations first and then computing stationary results of the electron transport along a device together with IV-curves.

We finally describe in Section 5 the stabilization towards equilibrium in time of the numerical results. We show that the results stabilize towards stationary values after plasma oscillations are damped. This oscillatory behavior is due to the highly doped contact regions and the charge neutrality condition imposed there. The damping rate of these oscillations becomes smaller for large applied bias, shorter channels or larger relaxation time; and thus stabilization time takes longer. These oscillations are explained physically due to the Landau damping phenomena predominant close to equilibrium where relaxation becomes less relevant.

2. Initial and boundary conditions: thermodynamical equilibrium

We detail in this section the computation of the initial condition for the scheme. A good initial seed will certainly lead to a faster and more stable stabilization towards the stationary state. Moreover, this initial guess should be the stationary solution in case no bias from source to drain is applied to the device, i.e., the thermodynamical equilibrium, which should be kept stationary by our scheme. Thus, for each p -subband, the thermodynamical equilibrium is given by

$$f_p^{eq}(x, k) = M(k)\rho_p^{eq}(x),$$

where the surface density ρ_p^{eq} is calculated by means of the Fermi levels ϵ_F^{eq} and the equilibrium potential energy ϵ_p^{eq} :

$$\rho_p^{eq}(x) = \frac{m_* k_B T_L}{\hbar^2} \exp\left(\frac{\epsilon_F^{eq}(x) - \epsilon_p^{eq}(x)}{k_B T_L}\right). \quad (5)$$

Taking into account the constraint of charge neutrality

$$\int_0^{L_z} N^{eq}(x, z) dz = \int_0^{L_z} N_D(x, z) dz$$

at contacts $x = 0$ and $x = L$, the following expression of the Fermi levels is obtained:

$$\epsilon_F^{eq}(x) = k_B T_L \log\left(\frac{\hbar^2}{m_* k_B T_L} \frac{\int_0^{L_z} N_D(x, z) dz}{\sum_{q=1}^{\infty} e^{-\frac{\epsilon_q^{eq}(x)}{k_B T_L}}}\right). \quad (6)$$

To compute the potential energy $\epsilon_p^{eq}(x)$ (energy levels) we still need to calculate the set of solutions of the Schrödinger–Poisson system (1), (2) at thermal equilibrium $(V^{eq}(x, z), \epsilon_p[V^{eq}(x, z)], \chi_p[V^{eq}(x, z)])$.

To solve the Schrödinger–Poisson block Eqs. (1), (2), (4), we need to compute the thermodynamical equilibrium to write appropriate boundary conditions. With this purpose, we need to deal with three different Schrödinger–Poisson problems, each corresponding to a different expression of the density $N[V]$.

Problem 1: Boundary potential. This is a 1D problem at contacts; for symmetry reasons, we just need to solve it at one contact, thus we choose the source $x = 0$. We want to obtain the profile for the potential to be used as Dirichlet condition at the contacts in the 2D problems. We call $V_{bp}(z)$ the solution of this problem. As boundaries, we impose homogeneous Neumann conditions at $z = 0$ and $z = L_z$; moreover, as the potential is defined up to a constant, we can impose $V_{bp}(0) = 0$ (symmetrically $V_{bp}(L_z) = 0$). Using the expressions Eqs. (4)–(6) the density, in this 1D case, is

$$N[V_{bp}](0, z) = \frac{\int_0^{L_z} N_D(0, \zeta) d\zeta}{\mathcal{Z}[V_{bp}](0)} \sum_{p=1}^{\infty} e^{-\frac{\epsilon_p[V_{bp}](0)}{k_B T_L}} |\chi_p[V_{bp}](0, z)|^2, \quad (7)$$

where the partition function has the general expression:

$$\mathcal{Z}[V](x) = \sum_{q=1}^{\infty} e^{-\frac{\epsilon_q[V](x)}{k_B T_L}}.$$

Problem 2: Thermodynamical equilibrium. Once we have computed the boundary potential, we can compute a thermodynamical equilibrium for the system when no bias from source to drain is applied. Nevertheless, we apply the gate potential. As in the previous problem, using the expressions Eqs. (4)–(6), the density has form

$$N[V_{eq}] = \frac{\int_0^{L_z} N_D(0, \zeta) d\zeta}{\mathcal{Z}[V_{bp}](0)} \sum_{p=1}^{\infty} e^{-\frac{\epsilon_p[V_{eq}](x)}{k_B T_L}} |\chi_p[V_{eq}](x, z)|^2, \quad (8)$$

where the fact that Fermi levels are constant in the device is used, because the same configuration at the source and drain is considered and no bias is applied. We remark that the neutrality condition of Problem 2 is preserved because $V_{bp}(z) = V_{eq}(\bar{x}, z)$ where $\bar{x} \in \{0, L_x\}$.

Problem 3: Time evolving potential. Once the thermodynamical equilibrium and the boundary potential are found we can write appropriate boundary conditions to solve the Schrödinger–Poisson–Boltzmann system Eqs. (1)–(3). In this way, while making the code progress in time, we need to update the potential during all the transition states: given the sub-band occupation factors $\{\rho_p\}_p$, the density is given by (4) and thus we need to solve the corresponding SP block.

Now, let us finally specify the boundary conditions for the Schrödinger–Poisson–Boltzmann system Eqs. (1)–(4), see Fig. 4. For problem Eq. (7) we impose homogeneous Neumann boundary conditions for $z = 0$ and $z = L_z$, i.e., $\frac{dV_{bp}}{dz}(0) = \frac{dV_{bp}}{dz}(L_z) = 0$. For problem (8) the values at contacts are given by V_{bp} as well as the values at gates are fixed by constant V_{GS} ; elsewhere homogeneous Neumann conditions are taken, i.e., $V_{eq}(x \in \{0, L_x\}, z) = V_b(z)$, $V_{eq}(x, z \in \{0, L_z\}) = V_{GS}$ at gates, and $\frac{dV_{eq}}{dz}(x, z \in \{0, L_z\}) = 0$ outside gates. For the SP block in each time iteration, boundary conditions are given by Dirichlet conditions at contacts and gates and Neumann conditions elsewhere: $V(0, z) = V_{eq}(z)$, $V(L_x, z) = V_{eq}(z) + V_{DS}$, $V(x, z \in \{0, L_z\}) = V_{GS}$ at gates, and $\frac{dV}{dz}(x, z \in \{0, L_z\}) = 0$ outside gates.

For the BTE, conditions to force the electrical neutrality for the entering particles are assumed at contacts $x = 0$ or $x = L_x$, see the discussion on [13, Section 2.1]. As usual, the outgoing particles are treated with homogeneous Neumann conditions. For the wave vector k there is no real border, since for large energies $|k|$ there should be no particle, i.e., for every t and x the distribution $f(t, x, k) \approx 0$ if $|k|$ is large. Therefore, homogeneous Neumann conditions are considered at these artificial boundaries as in [13].

3. Numerical schemes

As usual, in order to deal with magnitudes of order zero, we first reduce the complete system to dimensionless coordinates. We assume invariance along the y -dimension, therefore the device spans over the (x, z) -plane. In Table 1 we show the dimensionless variables taken into account, magnitudes with tilde are meant with dimensions, otherwise they are scaled.

The BTE, after the dimensionless process, reduces to

$$\frac{\partial f_p}{\partial t} + 2C^V k_1 \frac{f_p}{\partial x} - C^V \frac{\partial \epsilon_p^{pot}}{\partial x} \frac{\partial f_p}{\partial k_1} = \frac{1}{\tau} (\rho_p M - f_p), \tag{9}$$

where τ is now the dimensionless relaxation time $\tau = \tilde{\tau}/t^*$, and the dimensionless Maxwellian reads $M(k) = \frac{1}{\pi} e^{-|k|^2}$. The Schrödinger–Poisson system, after adimensionalization, reads

$$-C^{S,1} \frac{d}{dz} \left[\frac{1}{m_*} \frac{d\chi_p}{dz} \right] - C^{S,2} [V + V_c] \chi_p = \epsilon_p^{pot} \chi_p, \tag{10}$$

$$- \text{div}[\epsilon_R \nabla V] = -C^P [N - N_D]. \tag{11}$$

Numerical values for all the parameters as well as a summary of all the dimensionless constants are given in Tables B.1 and B.2.

Therefore, in the following we focus on showing the details of the numerical solver for the system (9)–(11). Two main blocks are concerned for the solution of the complete model:

- the BTE-block (Boltzmann transport equation) by splitting techniques or finite-differences schemes, see Section 3.2.
- the SP-block (Schrödinger–Poisson) by Newton–Raphson iterations, see Section 3.1.

The computational domain is discretized into a tensor product mesh, and a uniform mesh is taken in each direction:

$$\begin{aligned} x_i &= i \Delta x \quad i = -N_{ghp}, \dots, N_x + N_{ghp} - 1 \\ (k_1)_l &= -k_{max} + l \Delta k_1 \quad l = -N_{ghp}, \dots, N_{k_1} + N_{ghp} - 1 \\ (k_2)_m &= -k_{max} + m \Delta k_2 \quad m = 0, \dots, N_{k_2} - 1, \end{aligned}$$

where $\Delta x, \Delta k_1$ and Δk_2 are the uniform steps for x, k_1 and k_2 variables, respectively, k_{max} is the maximum values for k -variables, which is fixed with the condition $e^{kin}(k_{max}, 0) = \alpha \bar{N}$, where $\alpha = 2.436946$ is an adimensionalized reference energy and \bar{N} is an integer empirically adapted to the problem to cover the support of f along its evolution. Due to the type of schemes considered for BTE, additional points (N_{ghp} ghost points) for the x and k_1 meshes have to be taken into account at the border.

3.1. Newton–Raphson scheme for the SP block

We face now to solve efficiently the Schrödinger–Poisson problem written with physical dimensions

$$S[V](\chi_p[V]) := -\frac{\hbar^2}{2} \frac{d}{dz} \left[\frac{1}{m_*} \frac{d\chi_p[V]}{dz} \right] - q(V + V_c) \chi_p[V] = \epsilon_p^{pot}[V] \chi_p[V], \tag{12}$$

$$- \text{div}(\epsilon_R \nabla V) = -\frac{q}{\epsilon_0} (N[V] - N_D), \tag{13}$$

$$N \text{ is a function of } V \text{ through } \left(\text{given data, } \{ \epsilon_p^{pot}[V] \}_p, \{ \chi_p[V] \}_p \right). \tag{14}$$

Table 1
Dimensionless parameters.

Adim.	Parameter with dimensions	Value
$\tilde{x} = l^* x, \tilde{z} = l^* z$	$l^* = L_x$	$20 \times 10^{-9} \text{ m}$
$\tilde{k} = k^* k$	$k^* = \frac{\sqrt{2m_e k_B T_L}}{\hbar}$	$5.824664 \times 10^8 \text{ m}^{-1}$
$\tilde{t} = t^* t$	$t^* = \text{“typical time”}$	10^{-14} s
$\tilde{V} = V^* V$	$V^* = \text{“typical Vbias”}$	1 V
$\tilde{\epsilon} = \epsilon^* \epsilon$	$\epsilon^* = \frac{\hbar^2 k^2}{2m_e} = k_B T_L$	$4.141951 \times 10^{-21} \text{ J}$
$\tilde{\rho} = \rho^* \rho$	$\rho^* = k^{*2}$	$3.392672 \times 10^{17} \text{ m}^{-2}$
$ \tilde{\chi} ^2 = \chi^* \chi ^2$	$\chi^* = \frac{1}{l^*}$	$2.000000 \times 10^7 \text{ m}^{-1}$
$\tilde{N} = N^* N$	$N^* = \rho^* \chi^*$	$6.785343 \times 10^{24} \text{ m}^{-3}$

A natural way to proceed seems the use of iterative methods by which we recursively update the potential V until we converge to the solution: starting from an initial guess V^{old} , and therefore $(\{\epsilon_p^{pot}[V^{old}], \chi_p[V^{old}], N[V^{old}]\})$, we can exploit Eqs. 12, 13 to update the potential to a new value V^{new} . The overall scheme is summarized in Fig. 2.

Remark 1. Even if the code is implemented dimensionless, in order to derive the correct equations, it is much easier to develop all the calculations with physical units and perform adimensionalization once the scheme has been completely written.

We describe now how each step of the iteration is performed:

Step 1 – Newton–Raphson (coupled system). Rewriting Eq. (13) as

$$-\text{div}(\epsilon_R \nabla V) + \frac{q}{\epsilon_0}(N[V] - N_D) = 0,$$

then we can restate the problem as looking for the zero point V of the operator $P[V]$ defined by

$$P[V] = -\text{div}(\epsilon_R \nabla V) + \frac{q}{\epsilon_0}(N[V] - N_D). \tag{15}$$

Since the x variable is just a parameter in all these problems, we omit the x -dependencies in all this step. Therefore, the potentials here are just written as functions of the variable z .

The classical way to approach the zero point of a function is the use of Newton–Raphson method: suppose we have a guess V^{old} , then the next guess V^{new} is expressed in terms of the previous one by

$$P[V^{old}] + dP(V^{old}, V^{new} - V^{old}) = 0.$$

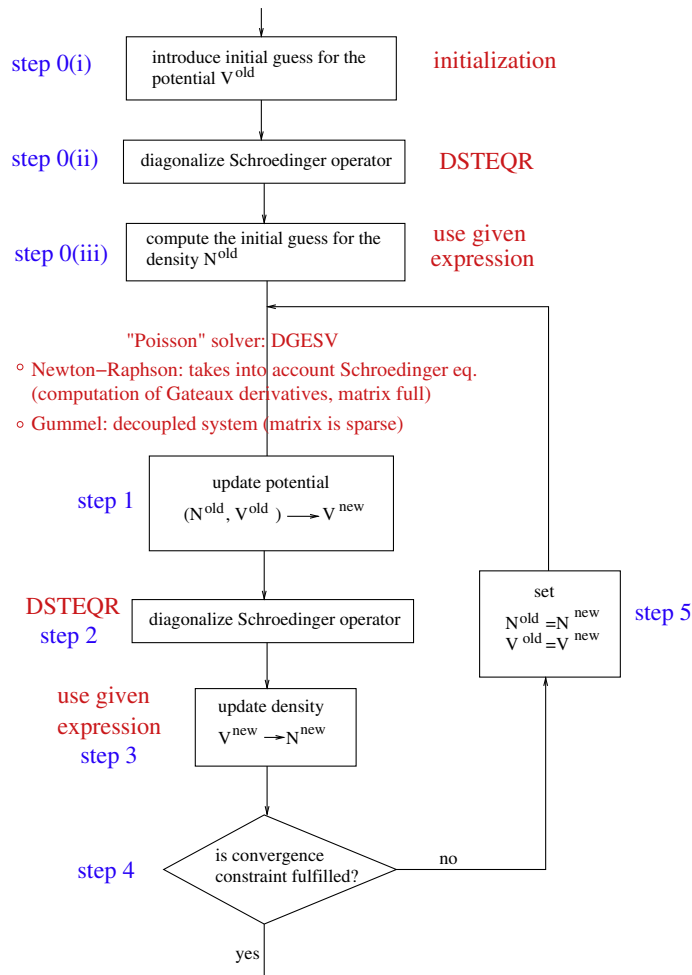


Fig. 2. The iterative solver for the Schrödinger–Poisson block.

As we are not dealing with real-valued functions, $dP(V, U)$ denotes the Gâteaux-derivative or directional derivative of P , at point V in direction U :

$$dP(V, U) = \lim_{t \rightarrow 0} \frac{P[V + tU] - P[V]}{t} = -\operatorname{div}[\epsilon_R \nabla U] + \frac{q}{\epsilon_0} dN(V, U).$$

In order to differentiate the density $N[V]$, we obtain the Gâteaux-derivatives of the eigenproperties $\{\epsilon_p^{\text{pot}}[V], \chi_p[V]\}_p$ of the eigenproblem Eq. (12).

We exploit the calculations in Appendix A by replacing the classical derivative $\frac{d(\cdot)}{dt}$ with the Gâteaux-derivative $d(\cdot)(V, U)$ and the vector scalar product $\langle \vec{v}, \vec{v}' \rangle = \sum_{i=1}^N v_i v'_i$ with that of $L^2(0, L_z)$, $\langle f, g \rangle = \int_0^{L_z} f(z)g(z) dz$ giving:

$$d\epsilon_p^{\text{pot}}(V, U) = \langle dS(V, U)\chi_p[V], \chi_p[V] \rangle,$$

$$d\chi_p(V, U) = \sum_{p'=1}^{\infty} \frac{\langle dS(V, U)\chi_p[V], \chi_{p'}[V] \rangle}{\epsilon_p^{\text{pot}}[V] - \epsilon_{p'}^{\text{pot}}[V]} \chi_{p'}[V].$$

This is a crucial point, because it is here that Eqs. (12) and (13) are fully coupled. In our case the Gâteaux-derivative of the functional in (12) is easily computed, $dS(V, U) = -qU$, and if we explicit the L^2 -scalar product $\langle \cdot, \cdot \rangle$, we can rewrite the derivatives

$$d\epsilon_p^{\text{pot}}(V, U) = -q \int_0^{L_z} U(\zeta) |\chi_p[V](\zeta)|^2 d\zeta,$$

$$d\chi_p(V, U) = -q \sum_{p'=1}^{\infty} \frac{\int_0^{L_z} U(\zeta) \chi_p[V](\zeta) \chi_{p'}[V](\zeta) d\zeta}{\epsilon_p^{\text{pot}}[V] - \epsilon_{p'}^{\text{pot}}[V]} \chi_{p'}[V].$$

Let us remark that since the Schrödinger operator is symmetric, the eigenvectors and the eigenfunctions are real.

We can now express the Newton–Raphson scheme in terms of the Gâteaux-derivative of the Poisson functional (15) as:

$$-\operatorname{div}[\epsilon_R \nabla V^{\text{new}}] + \frac{q}{\epsilon_0} dN(V^{\text{old}}, V^{\text{new}} - V^{\text{old}}) = -\frac{q}{\epsilon_0} (N[V^{\text{old}}] - N_D). \tag{16}$$

The explicit calculation of the Gâteaux derivative of the density has the form

$$dN(V, U) = \int_0^{L_z} \mathcal{A}[V](z, \zeta) U(\zeta) d\zeta.$$

Then, the scheme (16) gives rise to a Poisson-like equation in which some extra non-local terms appear. Now, writing the final result in dimensionless units, we get

$$-\operatorname{div}[\epsilon_R \nabla V^{\text{new}}] + C^N \int \mathcal{A}[V^{\text{old}}](z, \zeta) V^{\text{new}}(\zeta) d\zeta = -C^P (N[V^{\text{old}}] - N_D) + C^N \int \mathcal{A}[V^{\text{old}}](z, \zeta) V^{\text{old}}(\zeta) d\zeta.$$

For completion, we give the expression of $\mathcal{A}[V] = \mathcal{A}_0[V] + \mathcal{A}_1[V]$, in adimensionalized units, for the three problems (7), (8) and (4):

$$(7) : \begin{cases} \mathcal{A}_0[V_{bp}](z, \zeta) = \frac{\int_0^{L_z/l^*} N_D(0, z) dz}{\sum_r e^{-\epsilon_r |V_{bp}|}} \sum_p \sum_{q \neq p} \frac{e^{-\epsilon_q |V_{bp}|} - e^{-\epsilon_p |V_{bp}|}}{\epsilon_p |V_{bp}| - \epsilon_q |V_{bp}|} \times \chi_p[V_{bp}](z) \chi_q[V_{bp}](z) \chi_p[V_{bp}](\zeta) \chi_q[V_{bp}](\zeta) \\ \mathcal{A}_1[V_{bp}](z, \zeta) = \frac{\int_0^{L_z/l^*} N_D(0, z) dz}{\left(\sum_r e^{-\epsilon_r |V_{bp}|}\right)^2} \times \left[\sum_{p, q} e^{-\epsilon_p |V_{bp}|} e^{-\epsilon_q |V_{bp}|} |\chi_p[V_{bp}](z)|^2 |\chi_p[V_{bp}](\zeta)|^2 \right. \\ \left. - \sum_{p, q} e^{-\epsilon_p |V_{bp}|} e^{-\epsilon_q |V_{bp}|} |\chi_p[V_{bp}](z)|^2 |\chi_q[V_{bp}](\zeta)|^2 \right] \end{cases}$$

$$(8) : \begin{cases} \mathcal{A}_0[V_{eq}] = \frac{\int_0^{L_z/l^*} N_D(0, z) dz}{\sum_r e^{-\epsilon_r |V_{eq}|}} \sum_p \sum_{q \neq p} \frac{e^{-\epsilon_q |V_{eq}|} - e^{-\epsilon_p |V_{eq}|}}{\epsilon_p |V_{eq}| - \epsilon_q |V_{eq}|} \times \chi_p[V_{eq}](z) \chi_q[V_{eq}](z) \chi_p[V_{eq}](\zeta) \chi_q[V_{eq}](\zeta) \\ \mathcal{A}_1[V_{eq}] = \frac{\int_0^{L_z/l^*} N_D(0, z) dz}{\sum_r e^{-\epsilon_r |V_{eq}|}} \sum_p e^{-\epsilon_p |V_{eq}|} |\chi_p[V_{eq}](z)|^2 |\chi_p[V_{eq}](\zeta)|^2 \end{cases}$$

$$(4) : \begin{cases} \mathcal{A}[V] = \sum_p \sum_{q \neq p} \frac{\rho_q - \rho_p}{\epsilon_p |V| - \epsilon_q |V|} \chi_p[V](z) \chi_q[V](z) \chi_p[V](\zeta) \chi_q[V](\zeta). \end{cases}$$

The divergence and gradient operators are approximated by alternate finite differences, in order to recover the classical centered scheme for the Laplacian, the integrals are computed through trapezoids or right-rectangles approximation and the linear system, which is full, is finally solved through a LAPACK routine called DGESV.

Step 1 – Gummel (decoupled system). As a completion we recall how the Gummel method works: the potential is updated by (in dimensional units)

$$-\operatorname{div}(\varepsilon_R \nabla V^{new}) + \frac{q}{\varepsilon_0} N[V^{old}] \frac{q}{k_B T_L} (V^{new} - V^{old}) = -\frac{q}{\varepsilon_0} (N[V^{old}] - N_D),$$

which becomes after adimensionalization

$$-\operatorname{div}(\varepsilon_R \nabla V^{new}) + C^N N[V^{old}] V^{new} = -C^{G,2} (N[V^{old}] (1 - C^{G,3} V^{old}) - N_D).$$

As well as before, the divergence and gradient operators are approximated by alternate finite differences, in order to recover the classical centered scheme for the Laplacian, the integrals are computed through trapezoids or right-rectangles approximation, but unlike Newton–Raphson scheme the system is sparse.

Remark 2. The difference with respect to the Newton–Raphson method is that this “Poisson” equation does not take into account the Schrödinger equation, which is why this system is called “decoupled” and the linear system is sparse: it does not feel any non-local effect.

Step 2 and Step 0(ii). Eq. (12) reads as the eigenvalue problem $S[V](\chi_p[V]) = \epsilon_p^{pot}[V] \chi_p[V]$, where $S[V]$ is the dimensionless Schrödinger functional

$$S[V](\cdot) = -\frac{1}{2} C^{S,1} \frac{d}{dz} \left[\frac{1}{m_*} \frac{d(\cdot)}{dz} \right] - C^{S,2} \times (\cdot).$$

We approximate the z-derivatives in alternate directions, in order to recover the classical centered three-point scheme for the Laplacian, then diagonalize the symmetric matrix by means of a LAPACK routine called DSTEQR.

Step 3 and Step 0(iii). Inject the given data and the eigenproperties into (14) to update the value of the density.

Step 4 – Stopping criteria. In the code, we have used as constraint to check convergence the L^∞ and L^2 -differences between the old and new potentials and densities with a tolerance fixed to 10^{-6} in dimensionless units.

3.2. Solvers for the BTE

The Boltzmann equations for each sub-band have been solved using two different schemes. The first one is based on a long tested strategy for semiclassical Boltzmann–Poisson systems using high-order WENO finite-difference schemes together with explicit third-order Runge–Kutta time discretizations, see [11–13] where the interested reader can find all the details.

The second possibility is a splitting scheme at two levels already used in [14] in the semiclassical setting:

- Time Splitting (TS) in the Boltzmann transport equation, in order to separate transports from collisions, i.e., we split (9) into

$$\frac{\partial f_p}{\partial t} + 2C^V k_1 \frac{\partial f_p}{\partial x} - C^V \frac{\partial \epsilon^{pot}}{\partial x} \frac{\partial f_p}{\partial k_1} = 0 \quad (17)$$

and $\frac{\partial f_p}{\partial t} = \mathcal{L}_p[f]$.

- Dimensional splitting (DS), in order to split the (x, k_1) -phase space when solving transports, i.e., we split (17) into

$$\frac{\partial f_p}{\partial t} + 2C^V k_1 \frac{\partial f_p}{\partial x} = 0 \quad \text{and} \quad \frac{\partial f_p}{\partial t} - C^V \frac{\partial \epsilon^{pot}}{\partial x} \frac{\partial f_p}{\partial k_1} = 0.$$

In this way, we reduce the schemes to solve numerically 1D linear advection equations and the collision equation is just a simple ODE to solve explicitly. We are in fact performing two splittings, one inside the other; the overall splitting scheme results in a seven-step scheme, as it is sketched in Fig. 3. The solver of the Boltzmann transport equation has to be coupled with the solver for the Schrödinger–Poisson block for updating all the band potential energies, which is why the scheme requires in fact eleven steps: the seven steps of the splitting plus four steps for updating the eigenproperties after each x-transport step. Remark that the other steps do not modify the surface densities ρ_p .

This kind of schemes has a long history in kinetic equations mainly used for Vlasov-like problems in plasma physics with the generic name of semi-lagrangian schemes, see [22] and the references therein. In order to keep locally a mass conservative method, semi-lagrangian methods were improved introducing the flux balance method (FBM) [22]. This method is based on following integral values along the characteristics backwards in time. More details about the FBM method can be found in [15,22]. Finally since the end points of backwards characteristics are not usually mesh-points a final interpolation at the level of the primitive function is needed to reconstruct the fluxes. Here, we use the fifth order Pointwise WENO-6,4 interpolation introduced in [15] where all details can be found by the interested reader.

Let us point out that all the numerical results shown in this paper give almost no difference in terms of equilibrium results and qualitative properties with either scheme for the transport/collision step. The advantage of the finite-difference

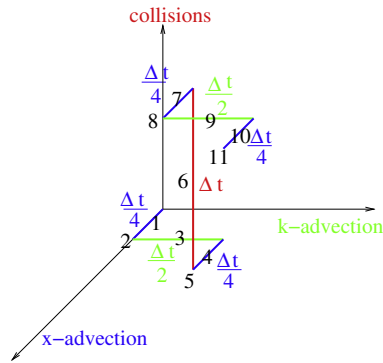


Fig. 3. A sketch of the splitting scheme: seven steps are due to the two successive splittings, and other four steps are needed after x -advection to update the band potential energies.

method being its high accuracy and the one of the splitting method its larger time stepping. We refer to [14] for a detailed discussion in the comparison of both methods.

3.3. Boundary conditions

The boundary conditions for the transport/collision equation and for the computation of the force field are resumed in Fig. 4.

As discussed in Section 2, we impose on the Boltzmann equation boundary conditions in order to force charge neutrality against thermal equilibrium at contacts as in [13]. They lead to

$$f_{p,-i,l,m}^n = \begin{cases} f_{p,0,l,m}^n & k_1 < 0 \\ \frac{\rho_p^{eq}(0)}{\rho_p^n(0)} f_{p,0,l,m}^n & k_1 \geq 0 \end{cases} \text{ for } i = 1, \dots, N_{ghp}$$

and

$$f_{p,N_x-1+i,l,m}^n = \begin{cases} f_{p,N_x-1,l,m}^n & k_1 > 0 \\ \frac{\rho_p^{eq}(L)}{\rho_p^n(L)} f_{p,N_x-1,l,m}^n & k_1 \leq 0 \end{cases} \text{ for } i = 1, \dots, N_{ghp}$$

Outgoing particles at contacts are treated with homogeneous Neumann conditions as well as for the artificial boundaries at $k_1 = \pm k_{max}$, i.e.:

$$\begin{cases} f_{p,i,-l,m}^n = f_{p,i,0,m}^n \\ f_{i,N_{k_1}-1+l,m}^n = f_{i,N_{k_1}-1,m}^n \end{cases} \text{ for } l = 1, \dots, N_{ghp}$$

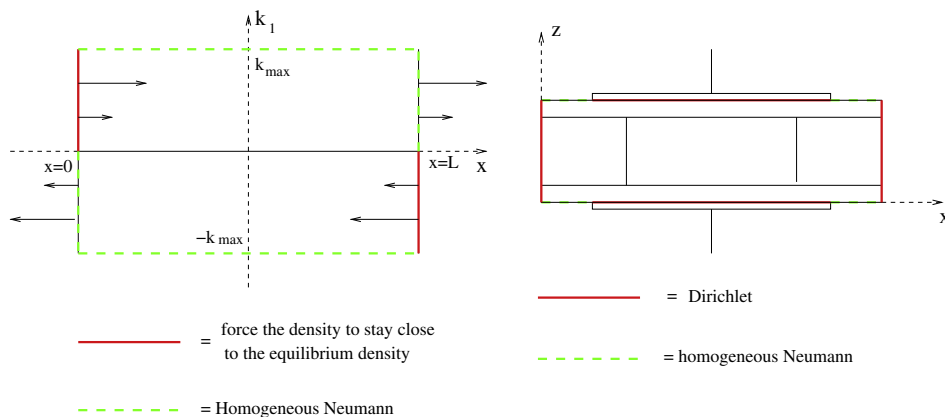


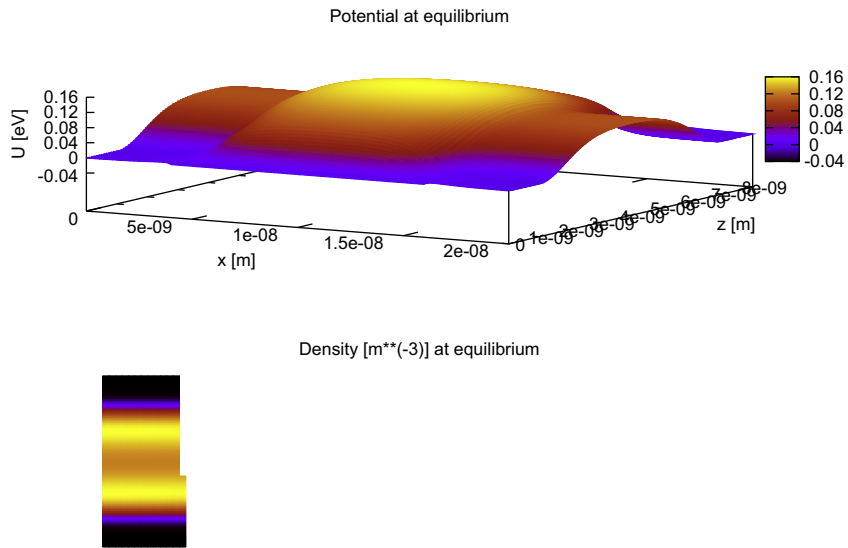
Fig. 4. Boundary conditions. Left: the Boltzmann transport equation. Right: the Schrödinger–Poisson block.

For the SP blocks, we impose numerically the Dirichlet or Neumann boundary conditions as discussed in Section 2 in a standard manner.

4. Numerical experiments

First, we simulate the thermodynamical equilibrium, which is our initial datum for the sequential Boltzmann–Schrödinger–Poisson system. We plot in Fig. 5 the thermodynamical equilibrium when no gate-source potential is applied. The number

As we explained in section 3 two different techniques could be used for simulating the first step of our SP solver: Newton–Raphson scheme or Gummel iteration. Therefore, we start by analyzing both methods.



Newton–Raphson versus Gummel. Newton–Raphson (NR) and Gummel methods give undistinguishable results and have proven stable, but the NR scheme, thanks to its ability of coupling Schrödinger and Poisson equations, converges in much less iterations and less time. In Fig. 6 we plot the convergence of both iterative methods towards the solution in order to fulfill as convergence parameter the stopping criteria in Section 3. NR requires 9 iterations while Gummel requires 23. In Table 2, the computational time of one step with both the NR and the Gummel methods is shown for different mesh sizes. As it can clearly be deduced NR is faster than Gummel in computational time to achieve convergence.

We can analyse how much faster NR is than Gummel, by performing a transient-states simulation in which, once computed the equilibrium, we apply the bias all of a sudden: the potential oscillates violently before stabilizing, so the iterative method at each step is initialized quite far from the solution.

In Fig. 7 we observe that NR, at each step, requires much less iterations than Gummel to converge. In the same figure we also plot the first update, the one in which the bias grows from 0 V to 0.2 V: Gummel requires more than 250 iterations to converge, while NR converges in 3. In Table 3, computational times for one step of NR and Gummel iterations are shown in this case for different mesh sizes. Since one NR unitary iteration is at most three times more expensive than the Gummel one, the overall simulation gain of the NR strategy is given by factors between 9 and 32 in the computed cases (see Fig. 7 and Table 3).

The choice of the effective mass. The choice of the effective mass influences the results in the sense that the smaller the effective mass is, the more separated the energy levels are. In Fig. 8 we show the energy levels and the occupations at the computed thermodynamical equilibrium for three different choices of the electron effective mass in a silicon crystal.

In the three-valley model, the occupations are obtained as an average value between the more and less occupied valleys, and the choice of $m_* = 0.50$, an average value, approximates this behavior.

Stationary solutions with applied bias. Once thermodynamical equilibrium is obtained in Fig. 5, it is considered as initial datum to study the time evolution until the stationary state. In order not to initialize every iterative method for the computation of the potential too far from the solution, the bias can be applied smoothly by means of a straight line, which joins

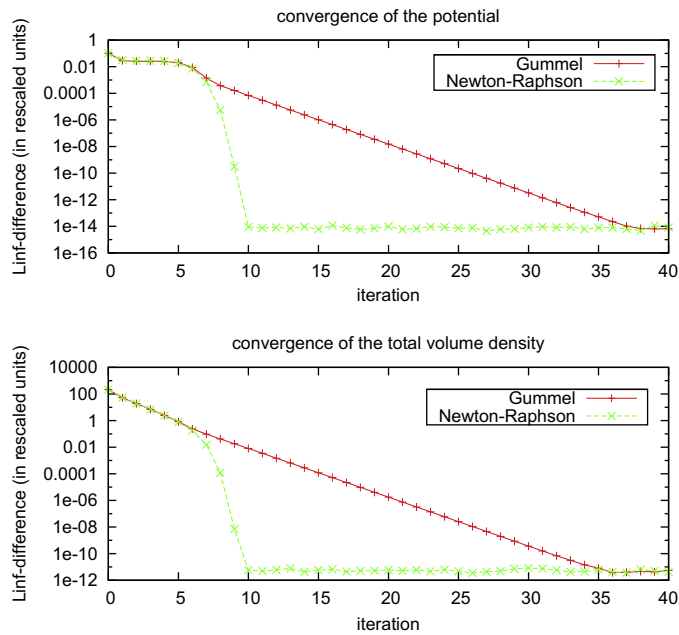
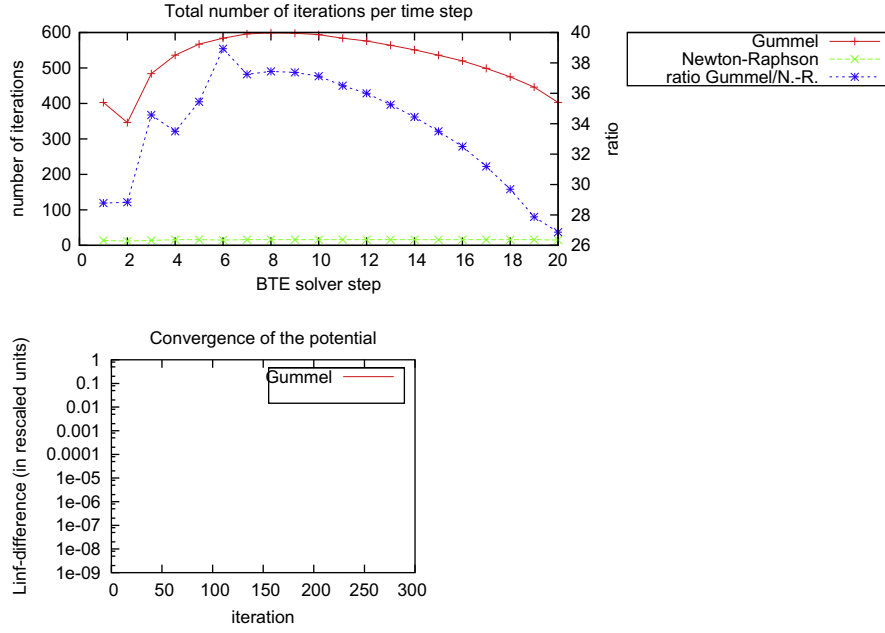


Fig. 6. Convergence of the iterative methods towards the thermodynamical equilibrium; On top: convergence parameter $\|V^{new} - V^{old}\|_{\infty}$ against iteration. Bottom: convergence parameter $\|N^{new} - N^{old}\|_{\infty}$ against iteration. Magnitudes are meant in dimensionless units.

Table 2

Approximate cost of one Newton–Raphson and one Gummel iteration for the computation of the thermodynamical equilibrium. Tests have been performed on a laptop computer with 2 GB RAM, 2.00 GHz frequency CPU, the code written in C language is compiled with the GNU C Compiler (gcc), the LAPACK routines compiled with gfortran-4.3.

(x, z)-mesh	NR 1-step cost (ms)	Gummel 1-step cost (ms)	Ratio
32 × 32	370	289	1.28
32 × 64	2230	1828	1.21
64 × 32	1346	1030	1.30
64 × 64	7780	6803	1.14



$V_{DS} = 0$ and $V_{DS} = V_{bias}$ with a slope as smooth as necessary. Although, this idea seems reasonable, we have observed that if the simulation converges to the stationary state, the velocity by which we apply the potential does not matter. Fig. 9 show the results for an applied bias of 0.2 eV. The first plot shows the first two sub-band energies and the mean drift velocity v_d computed in terms of f_p and the total surface density ρ by

$$\rho(x) = \sum_{p=1}^{\infty} \rho_p(x) \quad \text{and} \quad \rho(x) v_d(x) = \frac{\hbar}{m_*} \sum_{p=1}^{\infty} \int k_1 f_p(x, k) dk. \quad (18)$$

The other plots show the distribution functions of the first two sub-bands at the three positions marked on the first plot. In these figures we can notice the effect of thermal and ballistic velocities.

The velocity of the electron gas is determined partly by the thermal velocity distributed around zero at equilibrium, and partly by the applied bias. At thermodynamical equilibrium the current is null and the velocity of the electron gas is distributed around zero following a Maxwellian

$$M(k) = \frac{\hbar^2}{2\pi m_* k_B T_L} \exp\left(-\frac{\hbar^2 |k|^2}{2m_* k_B T_L}\right).$$

When we apply a bias, the particles, driven by the potential energies, acquire a velocity to flow from the source to the drain. When the stationary state is reached, the current becomes constant; as for the drift velocity, the particles are accelerated inside the channel: the larger the potential drop is, the more accelerated they will be. In the sketches of the pdf we can observe that inside the channel the distribution has two peaks: one for the thermal velocity and one for the ballistic velocity v_B , which would be given without energy dispersion by $\frac{1}{2} m_* v_B^2 = qV_{DS}$, thus $v_B = \sqrt{\frac{2qV_{DS}}{m_*}}$. In order to guarantee that the range of k is large enough and thus to choose N , we look at the value of $\frac{v_B m_*}{\hbar^2}$ and we call it $|k|_B$ and obtain the kinetic energy associated to this value: $\epsilon_B^{kin} = \frac{\hbar^2 |k|_B^2}{2m_*}$.

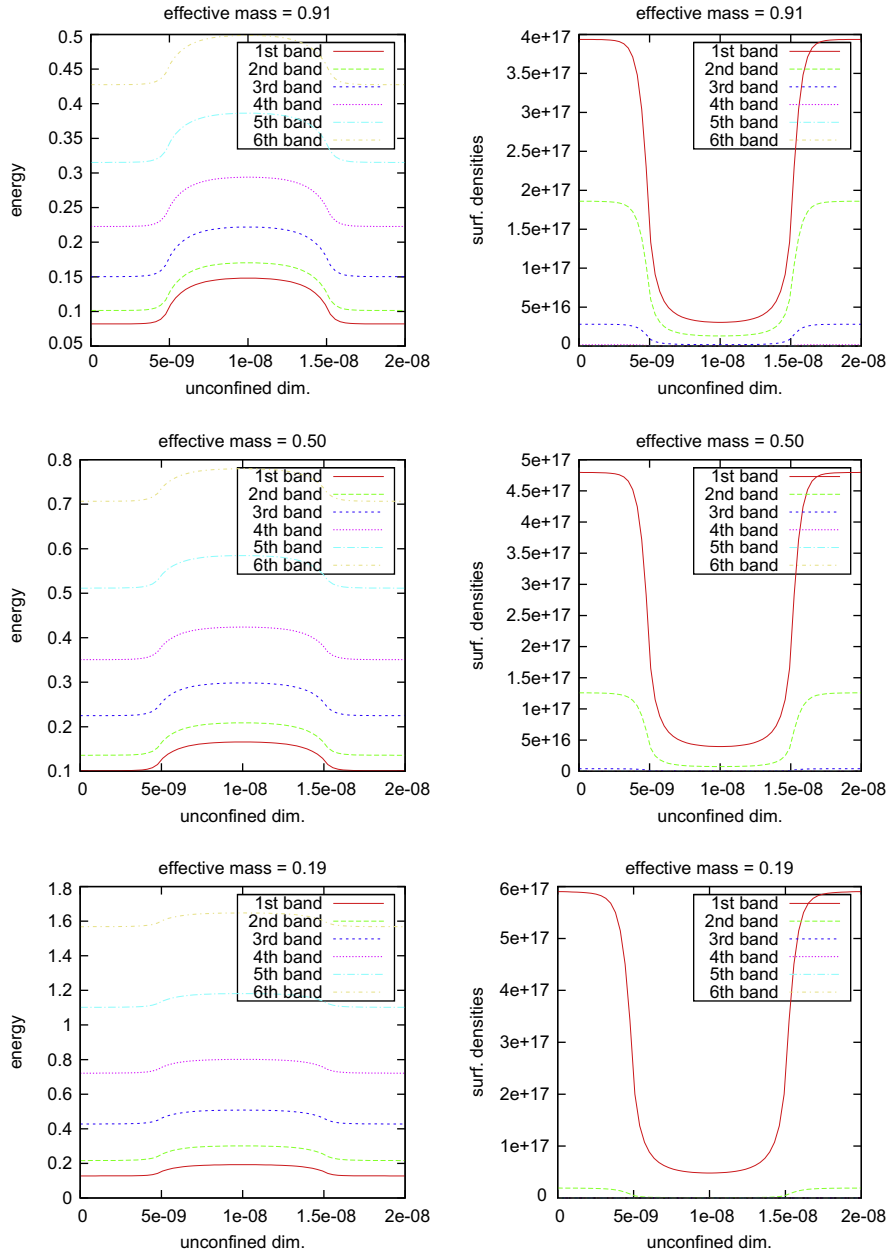


Fig. 8. Thermodynamical equilibrium computed using a one-valley band-structure, for three different choices of the electron effective mass. Left column: the band potential energies (in eV). Right column: the surface densities (in m^{-2}).

I–V curves and equilibration trend. We present the results on *I–V* curves in Fig. 10; they have been obtained by taking increasing bias steps of 0.02 V: after applying some bias, we keep computing until the stopping criteria is met, then this stationary state is used to initialize the code for a supplementary 0.02 V bias, and so on. The stopping criteria is on the adimensionalized density:

$$\|N^{new} - N^{old}\|_{L^\infty[(0,L_x) \times (0,L_z)]} < 10^{-4}.$$

In Fig. 11, we plot the evolution of the total charge, i.e., the scalar magnitude representing the total number of free electrons inside the device, and the average temperature given by $\frac{1}{L_x} \int_0^{L_x} T(x) dx$ where the position-dependent temperature is given by:

$$T(x) = \frac{\hbar^2}{2m_e k_B \rho(x)} \left\{ \sum_{p=1}^{\infty} \int |k|^2 f_p(x, k) dk - \frac{m^2}{\hbar^2} v_d^2(x) \rho(x) \right\}, \tag{19}$$

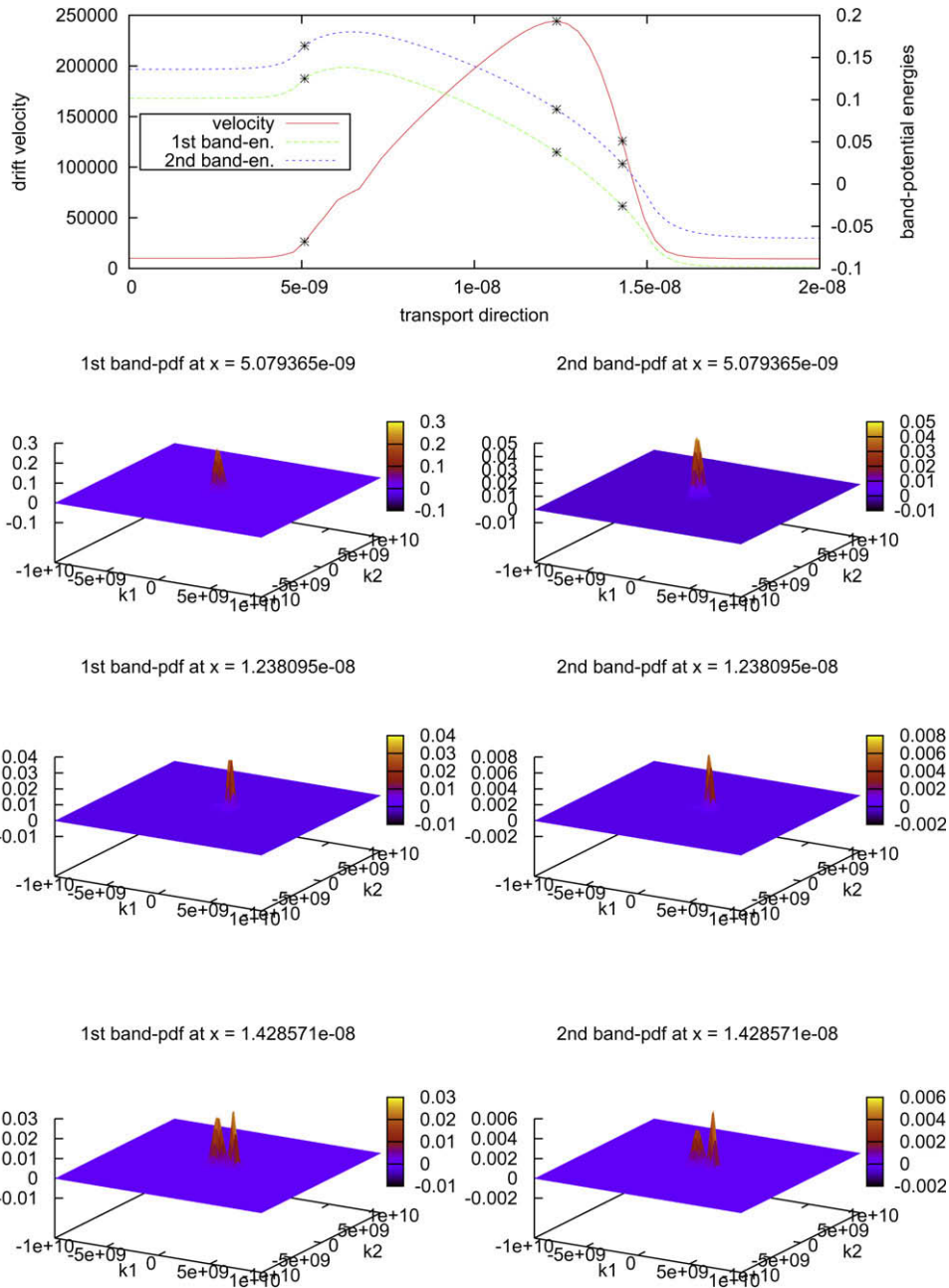


Fig. 9. Distribution function at the stationary state at three different point inside the channel. The V_{bias} is 0.2 eV, the grids in the (x, z, k_1, k_2) -space is $64 \times 64 \times 100 \times 100$, the time stepping $\Delta t = 2 \times 10^{-15}$ s with FBM method.

where ρ and v_d are the total surface density and mean drift velocity defined in Eq. (18).

We observe that before any stabilization the magnitudes oscillate periodically in time, and that as the bias increases the stabilization requires more and more effort: the damping rate of the amplitude decreases and the stabilization times increase. All the other magnitudes, scalar, macroscopic and microscopic, show the same behavior: damped oscillations and exchanges between potential and kinetic energies, increasing difficulties for increasing biases. The same behavior also happens for shorter channel lengths.

In order to visualize these oscillations, in Fig. 12 we have plotted how two macroscopic magnitudes, first band potential energy and density, oscillate in time at three different positions: in the drain contact, in the middle of the channel and in the middle of the source contact. We observe that the largest oscillations appear in the drain contact, since the carriers start to flow away from there. We have also plotted the shape of the first band potential energy $\epsilon_1(x)$ and of the kinetic energy $\frac{1}{2} m_e v_d^2(x)$ at different times to visualize the exchanges between kinetic and potential energies.

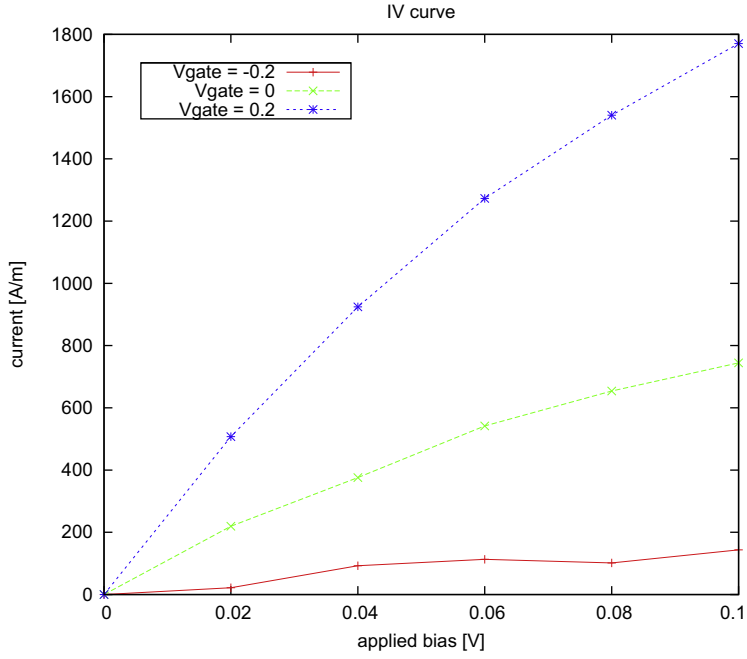
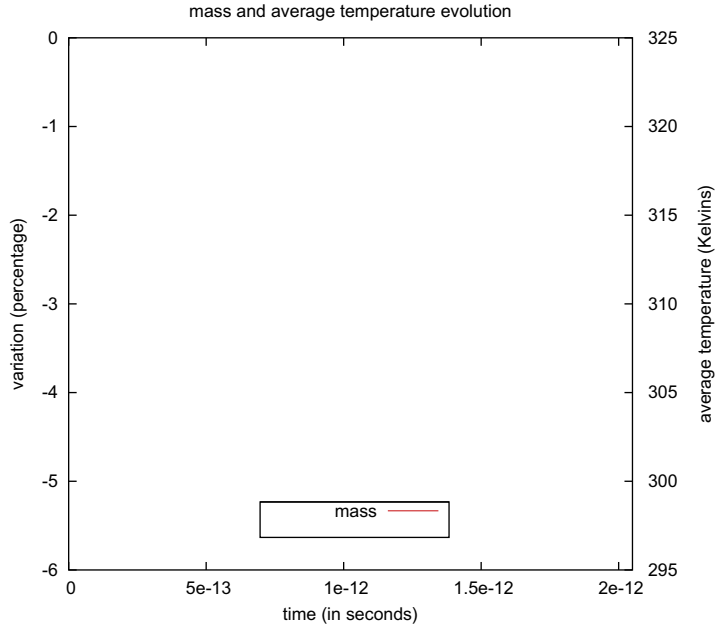


Fig. 10. I - V curve: shows the current at the stationary state against the applied drain-source bias. Refers to a 10 nm channel MOSFET, simulated with a $64 \times 64 \times 100 \times 100$ -mesh in the (x, z, k_1, k_2) -space, $\Delta t = 2 \times 10^{-15}$ s, $N = 120$.



We can theoretically expect the appearance of these oscillations. In fact, they are classically known in plasma physics literature [27,33] as *plasma oscillations*, whose frequency is given by

$$\omega_p = \sqrt{\frac{q^2 N_e}{\epsilon_R \epsilon_0 m_*}}, \quad (20)$$

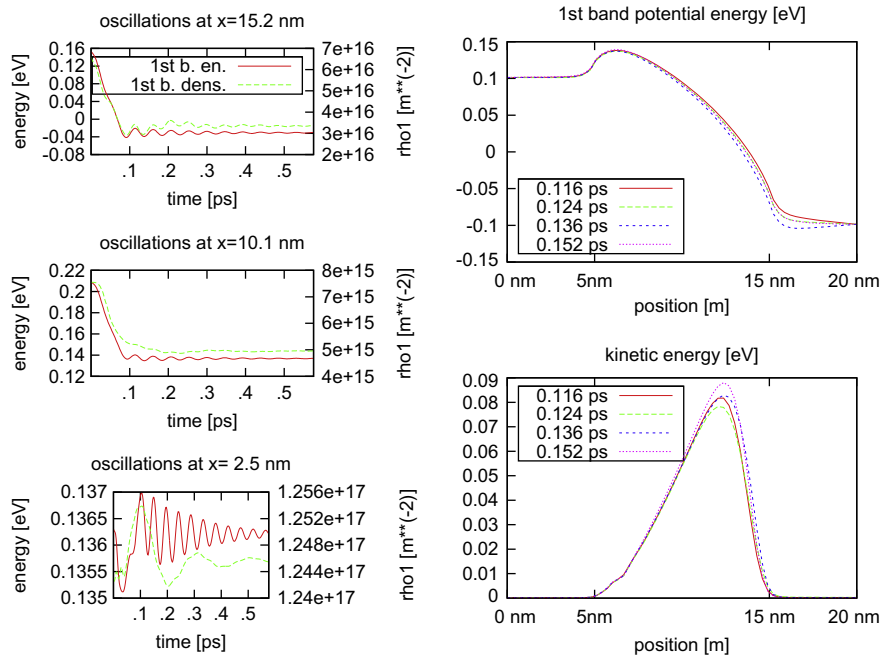


Fig. 12. A visualization of the energy exchanges in the case of a 0.2 V bias. Left column: the evolution in time of the first band potential energy and first band surface density for three fixed positions $x = 2.5$ nm, $x = 10.1$ nm and $x = 15.2$ nm. Right column: the shape of the first band potential energy $\epsilon_1(x)$ (top) and kinetic energy $\frac{1}{2}m_e v_d^2(x)$ (bottom) at four different instants.

where N_e is the average volume density of electrons

$$N_e = \frac{1}{L_x L_z} \int_0^{L_z} \int_0^{L_x} N(x, z) dx dz.$$

When some amount of charge is displaced with respect to the thermodynamical equilibrium, the Coulomb force makes the system oscillate while trying to equilibrate. These phenomena are only visible at nano-scale and high doping profiles in semiconductors, which is why no extensive studies have been performed yet.

In order to compute the expected values of the plasma frequency, we shall use the electron density at thermodynamical equilibrium $N^{eq}(x, z)$ for the estimate of the expected plasma frequency.

In order to check how the electron concentrations influence the oscillation frequency, we have performed tests with different values for the highly doped zones. Furthermore, we have changed the dielectric constant ϵ_R just for the purpose of measuring the change in the oscillation frequency. More precisely, we have multiplied by a factor the doping or the dielectric constant, and thus using Eq. (20), we know the precise expected ratio of increase in their frequency. In Table 4, we have the values of the numerically obtained frequency ω_{num} , the theoretical value ω_p from Eq. (20) based on the computed N_e and the numerical and theoretically expected ratio. Numerical ratio is calculated as it was indicated in the table, while theoretically expected ratio is known directly using Eq. (20) and taking as reference the first value of ω_p in the table. The numerical frequency ω_{num} is obtained by an a posteriori signal processing through the FFTW (the fastest Fourier transform in the west).

The appearance of these oscillations seems related to the scale of the device and not confinement or quantum effects: we have performed a simulation of 10 nm device through a completely classical Boltzmann–Poisson solver and we have observed a similar behavior, as well as longer devices of 20 nm and 30 nm simulated through our solver equilibrate faster. Moreover, the damping of these oscillations seems to be due to the Landau damping, naturally described through a kinetic-

Table 4

Numerically-computed oscillation frequencies. ω_p is the expected frequency and ω_{num} is the numerical frequency. The meshes are $50 \times 50 \times 50 \times 50$ in the (x, z, k_1, k_2) -space.

$N_D^{high} (\times 10^{26} \text{ m}^{-3})$	ϵ_R	m_*	$N_e (\times 10^{26} \text{ m}^{-3})$	$\omega_{num} (\times 10^{14} \text{ s}^{-1})$	$\omega_p (\times 10^{14} \text{ s}^{-1})$	Ratio $\frac{\omega_{num}}{\omega_{ref}}$	Expected ratio
1	11.7	0.5	.400	$\omega_{ref} = 1.344$	1.475	1	/
2	11.7	0.5	.783	2.051	2.064	1.52	$\sqrt{2}$
4	11.7	0.5	1.544	2.813	2.899	2.09	2
1	5.85	0.5	.400	1.848	2.086	1.37	$\sqrt{2}$

level solver, because even without any scattering the oscillations die off and the system equilibrates; the relaxation time should theoretically improve the equilibration by reducing the decay rate, but does seem to play a relevant rôle.

These tests support the statement that the oscillations which we observe are plasma oscillations. The appearance of these oscillations makes the computations of asymptotic equilibrium computationally expensive since we have to compute for longer times and smaller time steps. This is due to the fact that we resolve the plasma frequency scale with our numerical scheme. An interesting issue is to propose computational methods filtering these plasma frequencies in order to compute the asymptotic equilibrium faster. These issues, related to asymptotically preserving schemes [3,19,20] will be further analyzed in future work.

5. Conclusions

We have proposed and implemented a fast method to solve the Schrödinger–Poisson block in a partially confined device. This is based on the use of a Newton–Raphson method that treats the Schrödinger–Poisson block as a really coupled system. We show that it converges in much less iterations, and thus, less computing time than Gummel iteration method.

Then, we have solved the fully coupled description of nano-MOSFETs by the Boltzmann–Schrödinger–Poisson system Eqs. (1)–(4) using deterministic methods for kinetic equations coupled to the previous SP block solver. This gives a fully deterministic time-dependent solver for these partially confined devices at the mesoscopic description.

We have shown several numerical tests including computations of thermodynamical equilibrium, time-dependent equilibration towards stationary states and current–voltage characteristics. We have also demonstrated that plasma oscillations appear in the equilibration trend for typical physical parameters of nano-MOSFETs.

Finally, we should point out that the band-structure of Si is not properly described by a one-valley parabolic model. Moreover, the scattering operator should be much more realistic than a simple relaxation operator. A detailed study of plasma oscillation in this situation should be considered. These issues are currently being taken into consideration and will be reported elsewhere.

Acknowledgments

JAC, MJC and FV acknowledge partial support from the project MTM2008-06349-C03-03 from MICINN (Spain). MJC and FV acknowledge partial support from the Ingenio-Mathematica program. FV acknowledges support from the Marie Curie Early Stage Network DEASE: MEST-CT-2005-021122 funded by the European Union. Part of this work was done while JAC was a visiting professor at the University Paul Sabatier. NBA acknowledges support from the project QUATRIN funded by the french National agency for research (ANR 2007-2011).

Appendix A. The eigenvalue problem for the matrix case

In this appendix we quickly review the formulae leading to the explicit Gateaux derivatives of the eigenproperties of problem (12) in the SP block. For simplicity we show the computation in the finite dimensional case, which can be easily extended to our problem using the orthonormal basis for $L^2(0, L_z)\{\chi_p = \chi_p[V](x, z)\}_p$ with the usual scalar product. Consider the parametrized eigenvalue problem

$$M(t)\chi_p(t) = \epsilon_p(t)\chi_p(t), \tag{A.1}$$

$$\langle \chi_p(t), \chi_{p'}(t) \rangle = \delta_{p,p'}. \tag{A.2}$$

Our goal is the obtention of explicit formulae for the derivatives with respect to t of the eigenproperties $(\chi_p(t), \epsilon_p(t))_p$. Differentiate (A.1):

$$\frac{dM}{dt}(t)\chi_p(t) + M(t)\frac{d\chi_p}{dt}(t) = \frac{d\epsilon_p}{dt}(t)\chi_p(t) + \epsilon_p(t)\frac{d\chi_p}{dt}(t). \tag{A.3}$$

Next, we span $\frac{d\chi_p}{dt}(t)$ on the orthonormal basis of eigenvectors (A.2) in the form

$$\frac{d\chi_p}{dt}(t) = \sum_{p' \neq p} \alpha_{p,p'} \chi_{p'}(t).$$

Take Eq. (A.3), consider its scalar product by $\chi_p(t)$ (we omit t -dependency): straightforward manipulations give

$$\begin{aligned} \left\langle \frac{dM}{dt} \chi_p, \chi_p \right\rangle + \left\langle M \frac{d\chi_p}{dt}, \chi_p \right\rangle &= \frac{d\epsilon_p}{dt} \langle \chi_p, \chi_p \rangle + \epsilon_p \left\langle \frac{d\chi_p}{dt}, \chi_p \right\rangle \\ \left\langle \frac{dM}{dt} \chi_p, \chi_p \right\rangle &= \frac{d\epsilon_p}{dt}. \end{aligned}$$

Take now Eq. (A.3) and consider its scalar product by $\chi_{p'}(t)$ (with $p' \neq p$); some manipulations give an explicit formula for $\alpha_{p,p'}$:

$$\left\langle \frac{dM}{dt} \chi_p, \chi_{p'} \right\rangle + \left\langle M \frac{d\chi_p}{dt}, \chi_{p'} \right\rangle = \frac{d\epsilon_p}{dt} \langle \chi_p, \chi_{p'} \rangle + \epsilon_p \left\langle \frac{d\chi_p}{dt}, \chi_{p'} \right\rangle$$

$$\frac{\left\langle \frac{dM}{dt} \chi_p, \chi_{p'} \right\rangle}{\epsilon_p - \epsilon_{p'}} = \alpha_{p,p'},$$

by which we finally have explicit expressions for the derivatives of the eigenproperties:

$$\frac{d\epsilon_p}{dt}(t) = \left\langle \frac{dM}{dt}(t) \chi_p(t), \chi_p(t) \right\rangle$$

$$\frac{d\chi_p}{dt}(t) = \sum_{p' \neq p} \frac{\left\langle \frac{dM}{dt} \chi_p(t), \chi_{p'}(t) \right\rangle}{\epsilon_p(t) - \epsilon_{p'}(t)} \chi_{p'}(t).$$

Appendix B. Physical constants and dimensionless numbers

See Tables B.1 and B.2.

Table B.1

Physical constants.

Physical constant	Value
Reduced Planck constant	$\hbar = 1.05457162853 \times 10^{-34}$ J s
Boltzmann constant	$k_B = 1.380650424 \times 10^{-23}$ J/K
Electron mass	$m_e = 9.1093821545 \times 10^{-31}$ kg
Silicon effective mass	$m_s = 0.5 m_e$
Mobility	$\mu = 0.12$ m ² /V s
Positive electron charge	$q = 1.602176487 \times 10^{-19}$ C
Vacuum dielectric permittivity	$\epsilon_0 = 8.854187817 \times 10^{-12}$ C ² /N m ²
Relative dielectric function	$\epsilon_R = 11.7$
Lattice temperature	$T_L = 300$ K

Table B.2

Dimensionless constants.

Dimensionless constant	Value
$C^V = \frac{\epsilon^* \tau}{\hbar k^* l^*}$	1.348615×10^{-2}
$C^{S,1} = \frac{\hbar^2}{\epsilon^* l^{*2} m_s}$	2.358024×10^{-3}
$C^{S,2} = \frac{qV^*}{\epsilon^*}$	3.868169×10^1
$C^P = \frac{eN^* l^{*2}}{V^* \epsilon_0}$	1.534770×10^{-5}
$C^N = \frac{q^2 l^* \tau}{\epsilon_0 \epsilon^*}$	4.749401×10^3
$C^{G,2} = \frac{(l^*)^2 N^* q}{V^* \epsilon_0}$	1.227816×10^2
$C^{G,3} = \frac{qV^*}{k_B T_L}$	3.868169×10^1

References

- [1] T. Ando, B. Fowler, F. Stern, Electronic properties of two-dimensional systems, *Rev. Mod. Phys.* 54 (1982) 437–672.
- [2] G. Bastard, *Wave Mechanics Applied to Semiconductor Heterostructures*, Les ditions de physique, 1996.
- [3] R. Belaouar, N. Crouseilles, P. Degond, E. Sonnendrücker, An asymptotically stable semi-lagrangian scheme in the quasi-neutral limit, *J. Scientific Computing*, in press.
- [4] N. Ben Abdallah, A hybrid kinetic-quantum model for stationary electron transport, *J. Statist. Phys.* 90 (1998) 627–662.
- [5] N. Ben Abdallah, P. Degond, I.M. Gamba, Coupling one-dimensional time-dependent classical and quantum transport models, *J. Math. Phys.* 43 (2002) 1–24.
- [6] N. Ben Abdallah, F. Méhats, N. Vauchelet, Analysis of a drift-diffusion-Schrödinger–Poisson model, *C.R. Acad. Sci. Paris, Ser. I* 335 (2002) 1007–1012.
- [7] N. Ben Abdallah, F. Méhats, N. Vauchelet, A note on the long time behavior for the drift-diffusion-Poisson system, *C.R. Acad. Sci. Paris* 10 (339) (2004) 683–688.
- [8] N. Ben Abdallah, F. Méhats, N. Vauchelet, Diffusive transport of partially quantized particles: existence, uniqueness and long-time behaviour, *Proc. Edinb. Math. Soc.* 2 (49) (2006) 513–549.
- [9] N. Ben Abdallah, M. Lazhar Tayeb, Diffusion approximation for the one dimensional Boltzmann–Poisson system, *Discrete Contin. Dyn. Syst. Ser. B* 4 (4) (2004) 1129–1142.

- [10] N. Ben Abdallah, F. Méhats, Semiclassical analysis of the Schrödinger equation with a partially confining potential, *J. Math. Pures Appl.* (9) 84 (5) (2005) 580–614.
- [11] J.A. Carrillo, I.M. Gamba, C.-W. Shu, Computational macroscopic approximations to the 1-D relaxation-time kinetic system for semiconductors, *Physica D* 146 (2000) 289–306.
- [12] J.A. Carrillo, I.M. Gamba, A. Majorana, C.-W. Shu, A WENO-solver for the transients of Boltzmann–Poisson system for semiconductor devices. Performance and comparisons with Monte Carlo methods, *J. Comput. Phys.* 184 (2003) 498–525.
- [13] J.A. Carrillo, I.M. Gamba, A. Majorana, C.W. Shu, 2D semiconductor device simulations by WENO-Boltzmann schemes: efficiency, boundary conditions and comparison to Monte Carlo methods, *J. Comput. Phys.* 214 (2006) 55–80.
- [14] J.A. Carrillo, A. Majorana, F. Vecil, A semi-lagrangian deterministic solver for the semiconductor Boltzmann–Poisson system, *Commun. Comput. Phys.* (2) (2007) 1027–1054.
- [15] J.A. Carrillo, F. Vecil, Nonoscillatory interpolation methods applied to Vlasov-based models, *SIAM J. Sci. Comput.* 29 (3) (2007) 1179–1206. electronic.
- [16] G. Curatola, G. Iannaccone, NANOTCAD2D: two-dimensional code for the simulation of nanoelectronic devices and structures, *Comput. Mater. Sci.* 28 (2003) 342–352.
- [17] J.H. Davies, *The Physics of Low Dimensional Semiconductors*, Cambridge University Press, Cambridge, UK, 1998.
- [18] P. Degond, Mathematical modelling of microelectronics semiconductor devices, in: *Some Current Topics on Nonlinear Conservation Laws*, AMS/IP Stud. Adv. Math., vol. 15, Amer. Math. Soc., Providence, RI, 2000, pp. 77–110.
- [19] P. Degond, F. Deluzet, L. Navoret, An asymptotically stable Particle-in-Cell (PIC) scheme for collisionless plasma simulations near quasineutrality, *C.R. Acad. Sci. Paris, Ser. I* 343 (2006) 613–618.
- [20] P. Degond, F. Deluzet, L. Navoret, A.-B.Sun, M.-H. Vignal, Asymptotic-Preserving Particle-in-Cell Method for the Vlasov–Poisson System near Quasineutrality, preprint.
- [21] P. Degond, A. El Ayyadi, A coupled Schrödinger drift-diffusion model for quantum semiconductor device simulations, *J. Comput. Phys.* 181 (2002) 222–259.
- [22] F. Filbet, E. Sonnendrücker, P. Bertrand, Conservative numerical schemes for the Vlasov equation, *J. Comput. Phys.* 172 (1) (2001) 166–187.
- [23] M. Galler, F. Schürer, A deterministic solver for the transport of the AlGaIn/GaN 2D electron gas including hot-phonon and degeneracy effects, *J. Comput. Phys.* 210 (2005) 519–534.
- [24] M. Galler, *Multigroup Equations for the Description of the Particle Transport in Semiconductors*, Series on Advances in Mathematics for Applied Sciences, vol. 70, World Scientific Publishing, 2005.
- [25] M. Galler, F. Schürer, A direct multigroup-WENO solver for the 2D non-stationary Boltzmann–Poisson system for GaAs devices: GaAs-MESFET, *J. Comput. Phys.* 212 (2006) 778–797.
- [26] F. Golse, F. Poupaud, Limite fluide des équations de Boltzmann des semi-conducteurs pour une statistique de Fermi-Dirac, *Asymptotic Anal.* 6 (2) (1992) 135–160.
- [27] R.J. Goldston, P.H. Rutherford, *Introduction to Plasma Physics*, IOP Publ., Bristol and Philadelphia, 1995.
- [28] J.M. Mantas, M.J. Cáceres, Efficient deterministic parallel simulation of 2D semiconductor devices based on WENO-Boltzmann schemes, *Comput. Meth. Appl. Mech. Eng.* 198 (2009) 693–704.
- [29] P.A. Markowich, C. Ringhofer, C. Schmeiser, *Semiconductor Equations*, Springer-Verlag, New-York, 1990.
- [30] M.S. Mock, *Analysis of Mathematical Models of Semiconductor Devices*, Advances in Numerical Computation Series, vol. 3, Boole Press, Dún Laoghaire, 1983.
- [31] F. Nier, A Stationary Schrödinger–Poisson System arising from the modelling of electronic devices, *Forum Math.* 2 (1990) 489–510.
- [32] E. Polizzi, N. Ben Abdallah, Self-consistent three-dimensional models for quantum ballistic transport in open systems, *Phys. Rev. B* 66 (2002) 245301-1–245301-9.
- [33] P.A. Sturrock, *Plasma Physics*, Cambridge University Press, Cambridge, 1994.
- [34] A. Trellakis, A.T. Galick, A. Pacelli, U. Ravaioli, Iteration scheme for the solution of the two-dimensional Schrödinger–Poisson equations in quantum structures, *J. Appl. Phys.* 81 (1997) 7880–7884.
- [35] N. Vauchelet, Ph.D. Thesis, Université Paul Sabatier, 2006.
- [36] C. Weisbuch, B. Vinter, *Quantum Semiconductor Structures*, Academic Press, San Diego, CA, 1991.